SPE 59312

Verification of a Complete Pore Network Simulator of Drainage and Imbibition

Tad W. Patzek[1], SPE Member

[1]University of California at Berkeley and Lawrence Berkeley National Laboratory; patzek@patzek.berkeley.edu, http://patzek.berkeley.edu

This paper was prepared for presentation at the 2000 SPE/DOE Improved Oil Recovery Symposium held in Tulsa, Oklahoma, 3–5 April 2000.

Abstract. Relative permeability and capillary pressure functions define how much oil can be recovered and at what rate. These functions, in turn, depend critically on the geometry and topology of the pore space, on the physical characteristics of the rock grains and the fluids, and on the conditions imposed by the recovery process. Therefore, imaging and characterizing the rock samples and the fluids can add crucial insight into the mechanisms that control field-scale oil recovery. The fundamental equations of immiscible flow in the imaged samples are solved, and one can elucidate how relative permeability and capillary pressure functions depend on wettability, interfacial tension and the interplay among viscous, capillary and gravitational forces. This knowledge enables one to answer questions such as: Can a change of injected brine salinity increase oil recovery and by how much? How much more oil would be recovered if advancing contact angles could be modified? Does water injection help to recover sufficiently more oil or is it just for pressure maintenance? How can water imbibition be enhanced and oil trapping limited? Can relative permeabilities be modified with a polymer or with a chemical agent, such as an electrolyte or surfactant? Can one rely on gravity drainage of oil films to increase recovery? These and many other questions may be answered through a combination of imaging and calculations presented here. This paper summarizes the development of a complete quasi-static pore network simulator of two-phase flow, "ANetSim," and its validation against Statoil's state-of-the-art proprietary simulator. ANetSim has been implemented in MATLAB® and it can run on any platform. Three-dimensional, disordered networks with complex pore geometry have been used to calculate primary drainage and secondary imbibition capillary pressures and relative permeabilities. The results presented here agree well with the Statoil simulations and experiments.

1. Introduction. The world works differently at different scales [1], and earth sciences must therefore rely on different methods of modeling the diverse earth systems that range in size from atoms and molecules to the whole planet. **Fig. 1** shows the characteristic volume scales encountered in computational earth sciences, and **Fig. 2** shows the corresponding time scales. The respective scales of interest in this paper are highlighted in yellow. Both figures underscore the need for an understanding of the interactions among the numerous characteristic scales in earth sciences and for the appropriate computational tools. In particular, it is apparent that the molecular level approach, such as the Lattice-Gas or Boltzmann methods [2], cannot be extended to describe rock cores, oil-reservoirs, contaminant plumes and the earth's crust. Conversely, a continuum description of a gas condensate reservoir will fail to describe the motion of individual gas molecules that condense into thin films covering the rock surfaces.

At the bottom of Fig. 1, there are volume scales characteristic of individual molecules and thin films. The typical sizes of the pores of interest in this paper range from 1 micron in clays to a millimeter in coarse sandstones. One cubic centimeter of reservoir sandstone may have 200,000 pores bodies, 500,000 pore throats, and when filled with two immiscible fluids, may contain some 2,000,000 corner-films of water in contact with the nonwetting fluid. A typical pore network consists of ten-twenty thousand pore bodies and pore throats, and has volume less than 0.1 cm^3 (10^{11} μm^3). Such a network is extracted from 3D micro focused X-ray CT images made of 30-1,000 μm^3 cubes or "voxels." Note that passing from the voxel to network description reduces the amount of information about the pore space by at least three orders of magnitude. A typical voxel in an aquifer or an oil reservoir is 0.001-10 m^3 (10^{15}-$10^{19}$$\mu m^3$). Passing from a pore-network to a reservoir-voxel description reduces the amount of information about the pore space by an additional factor of 10^4-10^8. In contrast, a core voxel obtained from standard X-ray CT has a volume that is almost equal to a typical pore-network. In fact, a large network with 500,000

pore bodies has been used recently to simulate corefloods in a heterogeneous carbonate [3]. This overlap establishes an important link between the pore network models and the interpretation of coreflood results. A characteristic gridblock size in a field-scale flow simulation ranges from decimeters to hundreds of meters, causing yet another astronomical loss of information about the pore space. Oilfield inter-well spacing ranges from tens of meters to several kilometers. We understand intuitively that "ghosts" of the pore structure should still be visible at the gridblock scale. The volume averaging methods that retain the shadows of the fine-scale structure are called *upscaling*.

The pore network model presented in this paper is quasi-static and percolation description is appropriate. Percolation is about connectedness [4]. P. G. de Gennes, winner of the 1991 Nobel Prize in Physics for his seminal work on the theoretical physics of disordered materials, has described [5] the percolation transition in the following way: “Many phenomena are made of random islands and in certain conditions, among the islands, one macroscopic continent emerges.”

Percolation phenomena are common in nature and occur in porous media (spontaneous imbibition without corner flow and with surface roughness), in multiphase systems (critical phenomena), in chemical systems (polymerization reactions), and in biological systems (the antibody-antigen immunological reactions). The special properties of a system, which emerge at the onset of macroscopic connectivity within it, are known as *percolation phenomena*.

In porous media, the invading fluid must be connected to the inlet to continue invading and the defending fluid must be connected to the outlet to be displaced. This dynamic percolation process, akin to following a movie, is called *invasion percolation* [6]. If clusters of the defending fluid can become disconnected from the outlet, we call this process *percolation with trapping* [7].

Primary drainage is a pure bond invasion-percolation problem, while imbibition is a problem in mixed invasion-percolation and ordinary percolation with trapping. The two processes are classified in **Fig. 3**. Previous studies, e.g., [8, 9], have demonstrated that pore geometry determines which imbibition mechanisms occur, **Fig. 4**. Experiments show that both wetting and nonwetting fluids can flow simultaneously, but with different velocities, in the same pore. The wetting fluid remains in the extreme corners of the pore cross-section and in the roughness of the walls. The existence of film flow of wetting fluid explains the richness of mechanisms involved in imbibition.

This paper is structured as follows. First, the salient features of the pore network description are discussed. Second, the pore-level description of drainage is summarized. Third, the imbibition mechanisms are discussed. Much of the pore-network description used in this paper follows that presented in [10]. Here only the differences of approach will be highlighted. The entire model presented in this paper has been described in detail elsewhere [11] and is being taught as a graduate course at UC Berkeley.

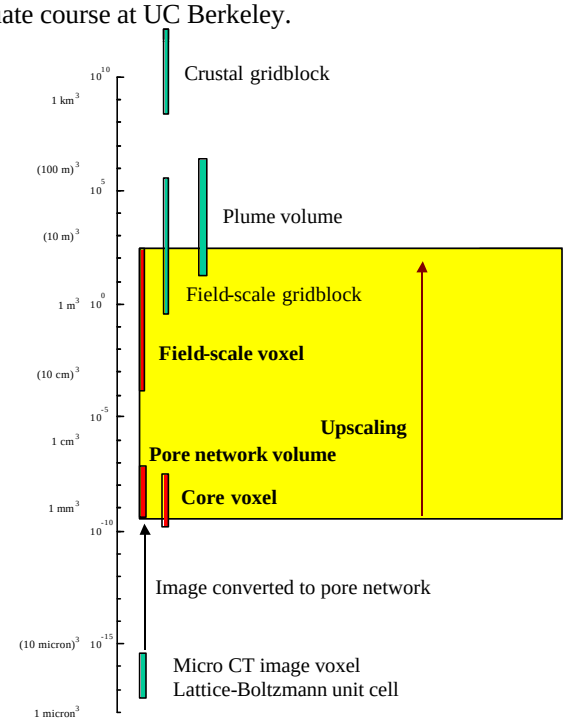

Fig. 1 - Characteristic volume scales in earth sciences.

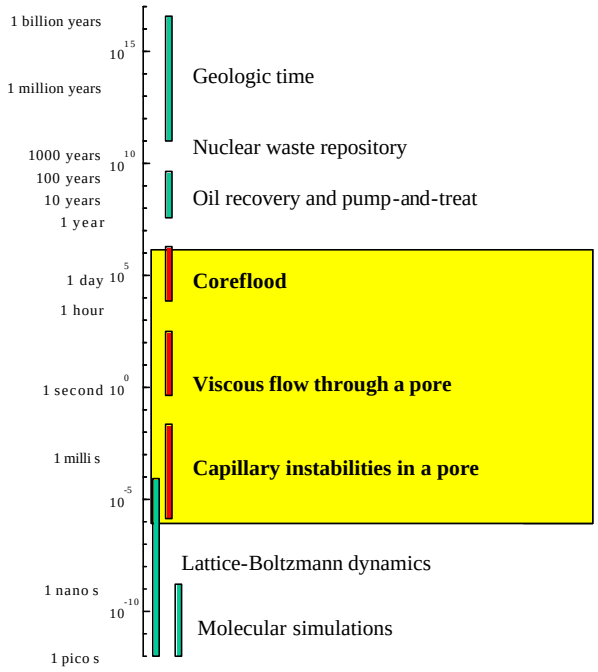

Fig. 2 – Characteristic time scales in earth sciences.

Flow type	Flow regime	Large/medium pores	Small pores
One-phase flow	Bulk flow	Effective medium approach	
Drainage	Bulk flow	Invasion percolation (IP)	
Imbibition	Bulk flow and corner flow	IP in dual network	Frontal drive compact growth
	Bulk flow and roughness flow	Bond percolation	Nucleation, compact cluster growth
Viscous flow	Stable	Flat interface	
	Unstable	Gradient governed growth or Diffusion limited aggregation (DLA)	

Fig. 3 – Various pore-level displacement mechanisms and related statistical models, adapted from [9].

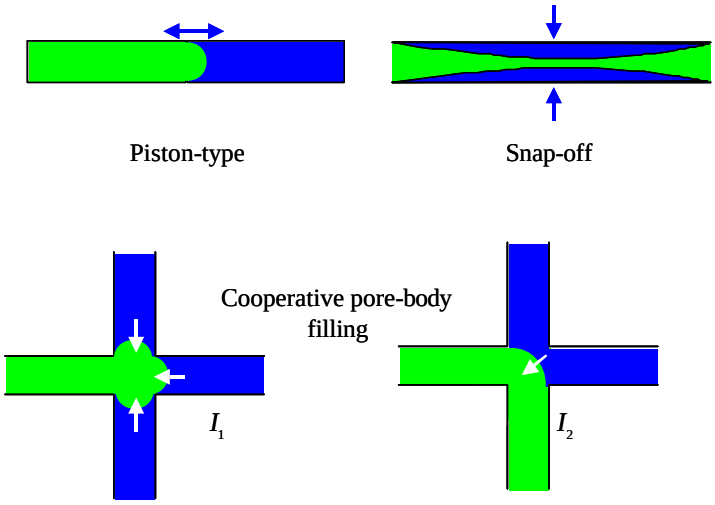

Fig. 4 – Pore level mechanisms in drainage (piston-type) and imbibition (all). I_1 and I_2 denote the cooperative pore-body filling with one and two pore throats filled with the nonwetting phase.

2. Pore network description. The three-dimensional pore network used here is shown in **Fig. 5**. This network represents a $(2.5\ \text{mm})^3$ sample of Bentheimer sandstone and consists of 3677 pore bodies (nodes or sites) and 8952 pore throats (links or bonds). The network connectivity varies, with zero to sixteen pore throats connected to a pore body. A random distribution of receding (0.009-0.05^0) and advancing (25-85^0) contact angles is imposed. Most of the pores are triangular in cross-section and their shapes have been determined, albeit somewhat non-uniquely, from image analysis. 146 pore bodies have square cross-sections and 35 are circular. 1159 pore throats are square and 789 are circular. There are 183 pore bodies connected to the inlet and 208 connected to the outlet. The network porosity is 0.234, its microporosity is 0.014, and the absolute permeability is 5149 md (0.3% error relative to Statoil).

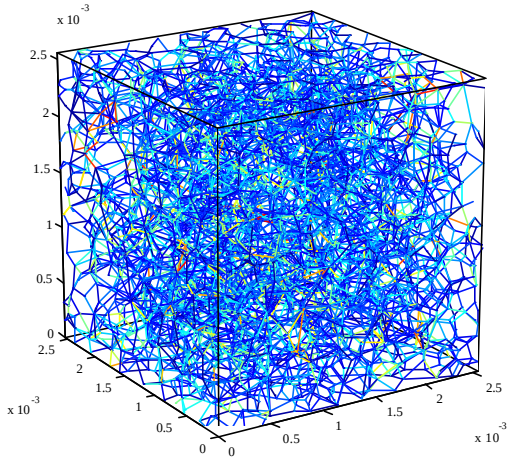

Fig. 5 - Three-dimensional network representation of a water-wet sandstone sample, the network description is courtesy of Statoil.

2.1 Pore shapes. Real pore bodies and pore throats have complex and variable cross-sections. Here we approximate them as cylindrical ducts of constant but arbitrary shapes of the cross-sections. This means that all pores in the network are translationally symmetric along the cylinder generators, **Fig. 6** and **Fig. 7**.

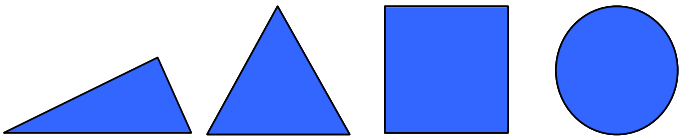

Fig. 6 – Typical cross-sections of flow ducts in the network.

The triangular tube geometry is determined through two parameters: the shape factor, G, and the inscribed circle radius, r. Given the corner half-angles, β_1, β_2 and β_3, we adopt a convention that $\beta_1 < \pi/4$ and $\beta_2 < \pi/4$ are the two corner half-angles subtended at the longest side of the triangle (its base). The pore cross-sectional area A and its perimeter P are expressed through Mason and Morrow's [12] "shape factor"

$$G = \frac{A}{P^2} = \frac{1}{4\sum_{i=1}^{3}\cot\beta_i} = \frac{1}{4}\tan\beta_1 \tan\beta_2 \cot(\beta_1+\beta_2). \quad (1)$$

For each G, only the triangular shapes between two limiting isosceles triangles, when $\beta_1 = \beta_2$ or $\beta_2 = \beta_3$, are admissible. The family of the limiting isosceles triangles is parameterized by the following angles:

$$b_{2,\min} = b_1 = b \quad \text{and} \quad b_{2,\max} = p/4 - b_1/2 = p/4 - b'/2, \quad (2)$$

where $0 \le b$ and $b' \le p/6$ are dummy variables. Obviously, a single value of G corresponds to a range of corner half-angles and therefore triangular shapes, **Fig. 8.**

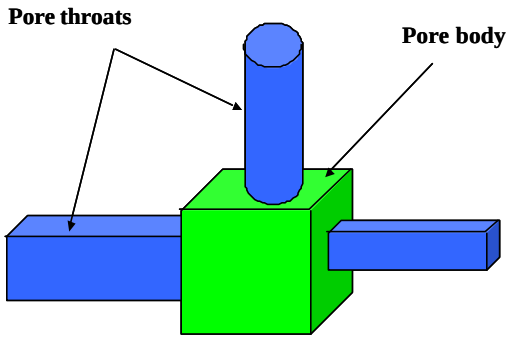

Fig. 7 – The network is assembled by snapping together the individual "Lego" ducts.

Given the shape factor G of a triangular duct, the corner half-angles may be chosen as follows:

(1) Find the bounds on b_2, $b_{2,\min} \le b_2 \le b_{2,\max}$, by inserting into Eq. (1) the values of b_2 from Eq. (2),

(2) Pick at random a value of $b_{2,\min} \le b_2 \le b_{2,\max}$,

(3) Use Eq. (1) to calculate the appropriate value of b_1,

(4) Calculate $b_3 = p/2 - b_1 - b_2$.

To find the left branch of the G-dome analytically, one may substitute $b_2 = b_1$ in Eq. (1) and solve for $x = \tan b_1$:

$$\Delta \equiv \left[-36G + \sqrt{-3 + 1296G^2}\right]^{1/3},$$

$$x = -\frac{i}{6}\left[-\frac{3^{2/3}(i+\sqrt{3})}{\Delta} + 3^{1/3}(\sqrt{3}-i)\Delta\right], \quad (3)$$

$$b_1 = \arctan(x),$$

where i is the imaginary unit. The right branch of the G-dome can also be obtained analytically by substituting into Eq.(1) $b_2 = p/4 - b_1/2$, and solving for $x = \tan(b_1/2)$:

$$\Delta \equiv \left[-1 + 3G\left(-9 - 36G + \sqrt{-3 + 1296G^2}\right)\right]^{1/3},$$

$$x = -\frac{1}{12G}\left[2 + 12G + \frac{(1 - i\sqrt{3})(1 + 18G)}{\Delta} + (1 - i\sqrt{3})\Delta\right], \quad (4)$$

$$b_2 = \frac{p}{4} - \arctan(x).$$

2.2 Hydraulic conductance. The unit flow channel is shown in **Fig. 9**. In laminar flow of two immiscible phases, the flow rate of fluid i, water or oil, between two connected nodes I an J is given by

$$q_{i,IJ} = \frac{g_{iJJ}}{l_{IJ}}(p_{i,I} - p_{i,J}), \quad i = w, o \quad (5)$$

where l_{IJ} is the spacing between the pore body centers and g_{iJJ} is the hydraulic conductance, $m^4/Pa-s$. To calculate the absolute permeability, we fill the network with a single fluid and index i disappears. We calculate the relative permeabilities of wetting and nonwetting phase by performing two separate calculations at several levels of capillary pressure (average wetting phase saturation). The first calculation is done for the wetting fluid, which spans the entire network, and the second one is restricted to the nodes and links invaded by the nonwetting fluid.

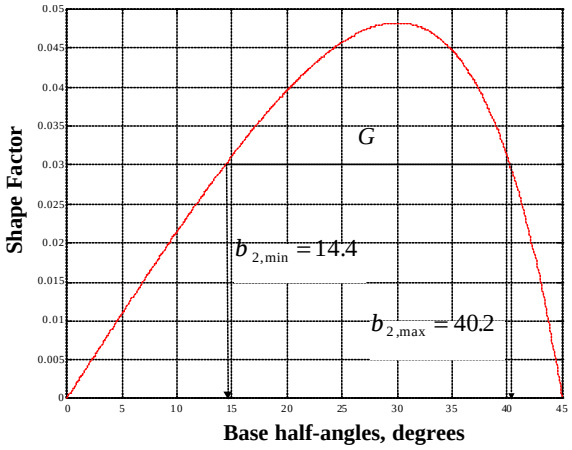

Fig. 8 – The shape factor or "G-dome" vs. base half-angles for triangular pores. The feasible values of the shape factor and the base half-angles are inside the dome. The dome consists of two branches, which meet at the peak. The left branch is parameterized by the dummy variable b in Eq.(2), while the right one by b'.

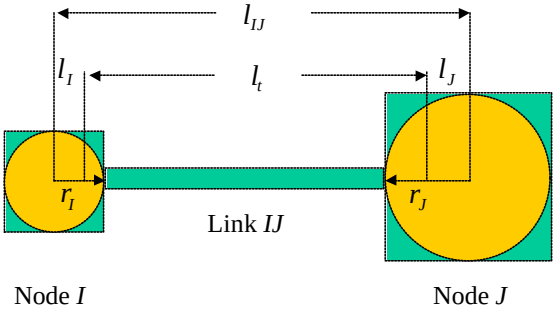

Fig. 9 - Geometry of a unit flow channel used to calculate the hydraulic conductance. The circles are cross sections of the largest spheres that can pass through each pore body; we call them the inscribed circles.

Flow resistances $\Re_i$ add; therefore, the overall flow conductance is the harmonic mean of the conductances of the connecting throat and its two pore bodies:

$$\Re_{IJ} = \Re_t + \frac{1}{2}\Re_I + \frac{1}{2}\Re_J$$
$$\frac{l_{IJ}}{g_{i,IJ}} = \frac{l_t}{g_{i,t}} + \frac{1}{2}\left(\frac{l_I}{g_{i,I}} + \frac{l_J}{g_{i,J}}\right) \quad i = w, o \tag{6}$$

The factor of ½ enters because only one half of each pore body resistance is allocated to the unit flow channel.

In steady state flow of incompressible immiscible fluids, mass conservation in each pore body can be described through the vanishing sum of the volumetric flow rates:

$$\sum_{\substack{\text{All throats } K \\ \text{connected to body } I}} q_{iJK} = 0, \quad i = w, o\,. \tag{7}$$

Equation (5) can be inserted into Eq. (7) to yield a system of linear equations in the unknown node (pore body) pressures. Dropping index *i*, the unknown pressures of the interior nodes are calculated from the following system of equations:

$$p_1\left(\sum_{K_1}\frac{g_{1,K_1}}{l_{1,K_1}}\right) - \sum_{K_1}\left(\frac{g_{1,K_1}}{l_{1,K_1}}\right)p_{K_1} = 0,$$
$$\cdots\cdots \tag{8}$$
$$p_{NN}\left(\sum_{K_{NN}}\frac{g_{NN,K_{NN}}}{l_{N\,N,K_{NN}}}\right) - \sum_{K_{NN}}\left(\frac{g_{N\,N,K_{NN}}}{l_{NN,K_{NN}}}\right)p_{K_{NN}} = 0,$$

where NN is the number of nodes.

2.2.1 Single-phase flow. The dimensionless hydraulic conductance of a duct with the equilateral triangle cross-section may be calculated analytically, e.g., [11]:

$$\tilde{g}_{\max} = \frac{gm}{A^2} = \frac{3}{5}G_{\max}\,, \tag{9}$$

where $G_{\max} = \sqrt{3}/36$. We assert that Eq. (9) approximates the dimensionless hydraulic conductance of any triangular cross-section duct characterized by an arbitrary shape factor *G*:

$$\tilde{g} = \frac{gm}{A^2} \approx \frac{3}{5}G\,. \tag{10}$$

The dimensionless conductances of the square and circular cross-section ducts are $0.5623G$ and $0.5G$, respectively. **Fig. 10** shows the dimensionless hydraulic conductances in single-phase flow in triangular, rectangular and elliptic ducts.

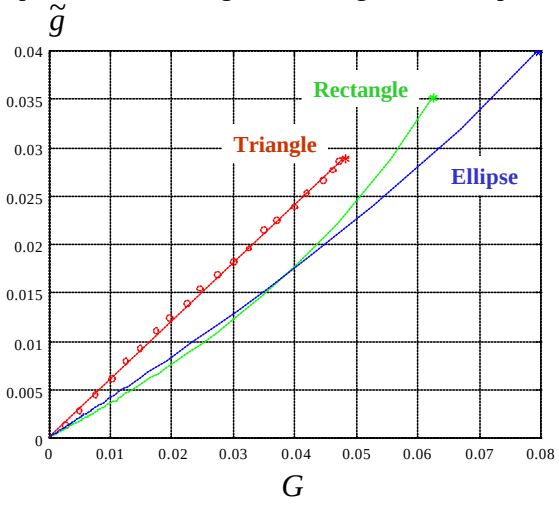

Fig. 10 - The dimensionless hydraulic conductance versus shape factor for one-phase flow in the triangular, rectangular and elliptic cross-section ducts. The stars denote the respective limiting values for equilateral triangle, square and circle. The triangle branch has been confirmed numerically, the rectangle and ellipse branches have been obtained analytically [11]. The numerical calculations (open circles) are from [10], their Fig. 8.

2.2.2 Two-phase flow. When a nonwetting fluid is present, the wetting fluid forms cylindrical filaments along the corners of the duct (sometimes loosely referred to as "corner films"), and is separated from the nonwetting fluid by translationally symmetric arc-menisci (AMs). Here we assume that each AM surface is laden with surfactants and rigid, resulting in no-slip boundary conditions along the pore walls and the meniscus. The dimensionless conductance of wetting fluid is defined as $\tilde{g}_w = g_w m_w / b^4$, where b is the meniscus-apex distance along the wall. The dimensionless corner flow conductances have been calculated elsewhere [13] for a variety of corner half-angles and contact angles, **Fig. 11**, using a high-resolution finite element method implemented in MATLAB [14].

With $b = 1$, the flow cross-sectional area and shape factor of the corner filament are calculated as follows:

$$A_w = \begin{cases} \sin b\,\cos b\,, & \text{if } q + b = p/2 \\ \left(\dfrac{\sin b}{\cos(q+b)}\right)^2\left(\dfrac{\cos q\,\cos(q+b)}{\sin b} + q + b - \dfrac{p}{2}\right) & \text{otherwise} \end{cases} \tag{11}$$

$$G = \begin{cases} \dfrac{A_w}{4(1+\sin b)^2}\,, & \text{if } q + b = p/2 \\ \dfrac{A_w}{4\left[1 - \sin b/\cos(q+b)(q+b-p/2)\right]^2} & \text{otherwise} \end{cases} \tag{12}$$

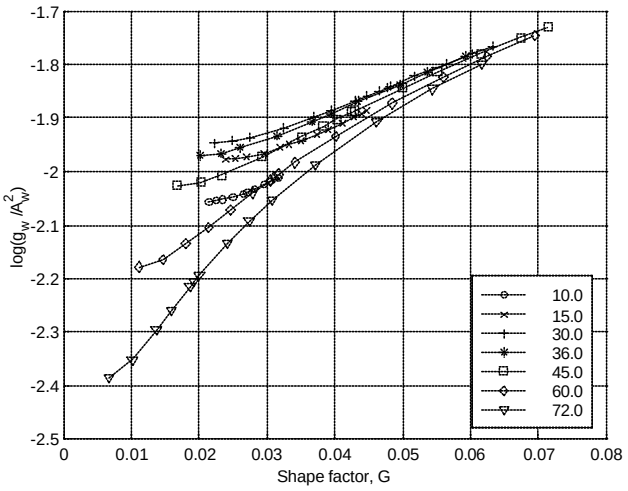

Fig. 11 – The logarithm of the ratio of dimensionless hydraulic conductance and corner filament area squared vs. the filament shape factor for corner half angles between 10 and 72^0.

We propose to scale the dimensionless hydraulic conductance of the corner wetting phase filaments as follows:

$$\tilde{g}_w = \ln\left(\frac{g_w}{A_w^2}\right)\left(\frac{1}{4p} - G\right)^{7/8}\cos^{1/2}\left(b - \frac{p}{6}\right) - 0.02\sin\left(b - \frac{p}{6}\right) \tag{13}$$

Equation (13) yields a universal curve when plotted versus shape factor, **Fig. 12**.

The structure of scaling in Eq. (13) can be explained as follows. All curves in Fig. 11 converge as the shape factor approaches that of circle, $G = 1/4p \approx 0.08$. Hence, the middle factor in the first term on the right side of Eq. (13) compensates for the deviation of shape factor from that of a circle. The third factor in the first term in Eq. (13) compensates for the deviation of corner geometry from that of an equilateral triangle corner. In Fig. 11, the curves for the 45^0- and 15^0 corner half-angle are close to each other, as are those for the 60^0- and 10^0 corner half-angles. The last term on the right side of Eq. (13) moves the $b = 72^0$ corner half-angle points onto the universal curve.

For each corner half-angle, the scaling in Eq. (13) produces an almost straight line. The slopes of the respective lines and their intercepts are very similar and, in turn, can be expressed as quadratic functions of the respective corner half-angles:

$$\tilde{g}_w = -0.5081 - 0.0022b - 0.0090b^2 + (6.5835 - 0.9951b + 0.9173b^2)G, \tag{14}$$

with b expressed in radians. The dimensional hydraulic conductance in corner flow of wetting phase is obtained by multiplying $\tilde{g}_w$ with the corresponding b^4 / m_w.

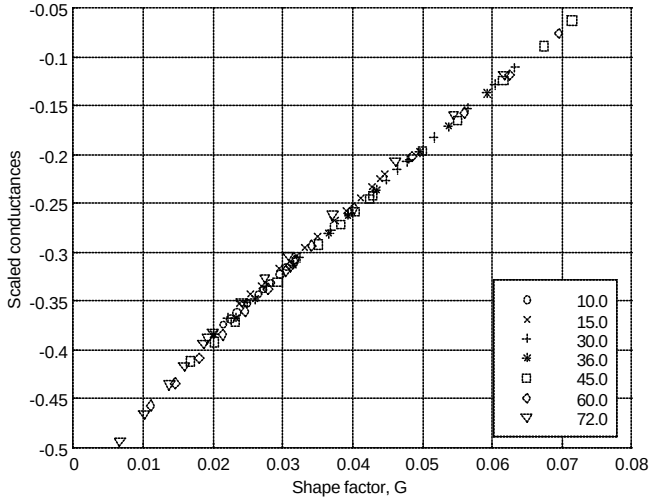

Fig. 12 - The scaled hydraulic conductance, Eq.(13), vs. shape factor.

Equation (13) is compared with the finite element results in **Fig. 13**. The mean absolute relative error of the approximation is 7.2%; however, for wide corner half-angles, 60^0 and 72^0, and large contact angles, the relative error is much larger, **Fig. 14**. Because the overall hydraulic conductance of wetting fluid is limited by the lowest individual filament conductances, the above-described weakness of the simple approximation given by Eq. (13) is acceptable.

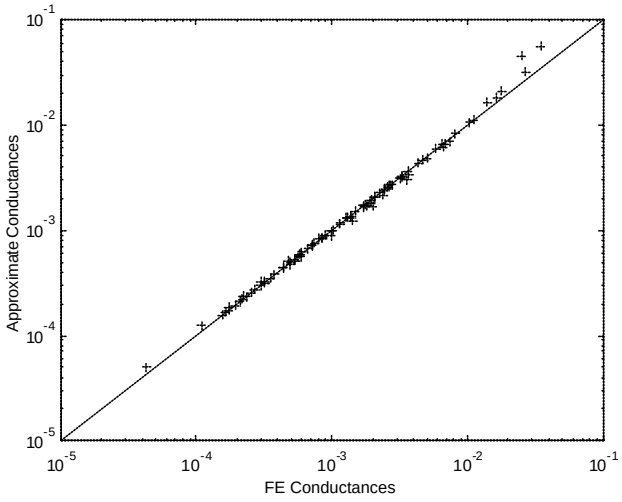

Fig. 13 - Approximation in Eq. (13) versus the finite element results for the no-slip case.

3. Drainage. We follow Øren *et al.'s* [10] generalization of Mason and Morrow's [12] expression for the threshold

capillary entry pressure in drainage. The receding contact-angle and the triangular pore shape are arbitrary. The Mayer-Stowe-Princen [15-18] (MS-P) method for calculating the threshold pressure relies on equating the curvature of the corner AMs to the curvature of the invading interface. The PV-work of displacing water from a pore translates into the threshold capillary entry-pressure, which is inversely proportional to the inscribed circle radius, and depends on the contact angle and pore shape. Piston-type drainage of a triangular pore is shown in **Fig. 15**, when there is no contact angle hysteresis, and the capillary pressures are made dimensionless with the inscribed circle radius and interfacial tension. Drainage is a bond invasion-percolation process. Therefore, the calculations are performed in order of increasing threshold capillary entry-pressures; only the accessible pore throats and their pore bodies are invaded at each step.

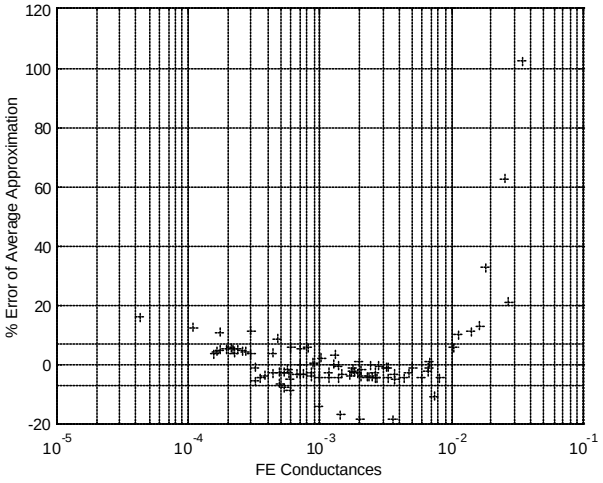

Fig. 14 - Percent relative error of the approximation in Eq. (13) increases for large corner half angles and large contact angles. The horizontal lines denote the mean absolute error.

The threshold capillary entry-pressure in primary drainage in a triangular pore can be expressed as

$$P^e_{cPD} = \frac{g}{r_d} = \frac{g}{r}\cos q_r (1+2\sqrt{pG})F_d(q_r, G, C_1), \qquad (15)$$

where g is the interfacial tension, and

$$F_d(q_r, G, C_1) = \frac{1+\sqrt{1-4GC_1/\cos^2 q_r}}{(1+2\sqrt{pG})}, \qquad (16)$$

is a function of the corner half-angles through

$$C_1 = \sum_{i=1}^{3}\left[\cos q_r \frac{\cos(q_r + b_i)}{\sin b_i} - \left(\frac{p}{2} - q - b_i\right)\right]. \qquad (17)$$

C_1 is not universal for a given G if the AMs are not present in all pore corners. Note that $F_d(q_r = 0, G, C_1) = 1$, regardless of how many pore corners have the water AM.

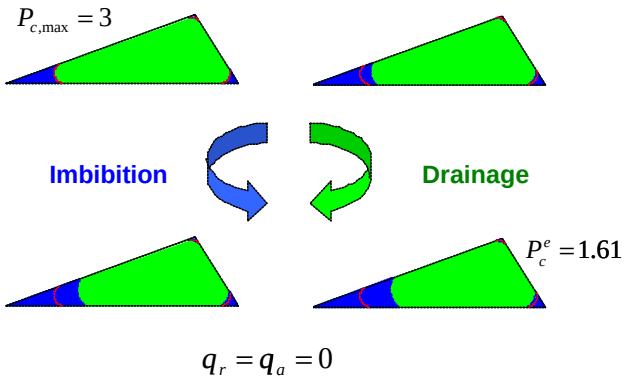

Fig. 15 – Drainage or imbibition without contact angle hysteresis in a triangular pore, G=0.01. Four frames from a single-pore mechanisms visualization simulator, "AMSim" [19], are shown.

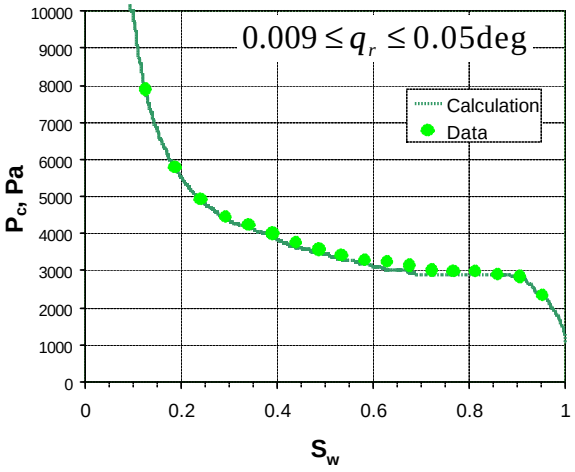

Fig. 16 – The calculated capillary pressure curve in primary drainage of the Bentheimer sandstone network vs. the Statoil results (circles) from P-E. Øren.

3.1 Drainage Results. Primary drainage of the sandstone network in Fig. 5 is shown in **Fig. 16**. ANetSim calculations compare very well with the Statoil model. The drainage relative permeability curves are shown in **Fig. 17**. The slight discrepancies between ANetSim and the Statoil simulator are most pronounced at intermediate oil saturations as shown in **Fig. 18** and **Fig. 19**. These discrepancies may be caused by

subtle differences in the invasion percolation algorithms and by different precision of the respective calculations (32/64 bits for ANetSim and 128 bits for Statoil).

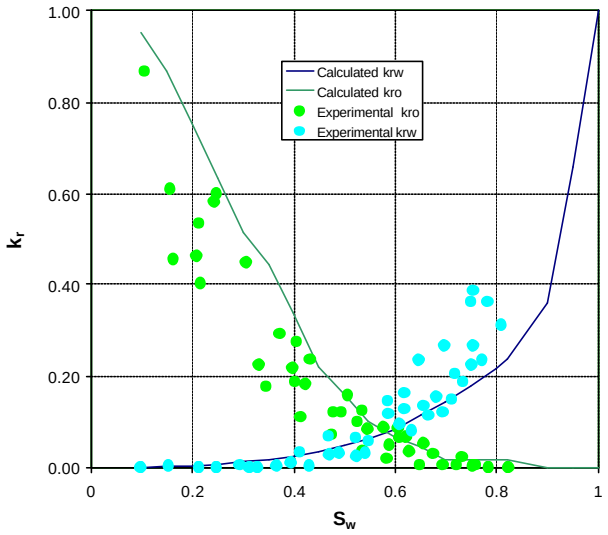

Fig. 17 – The relative permeability curves in primary drainage of the Bentheimer sandstone network vs. Statoil experiments from [10], their Fig. 14.

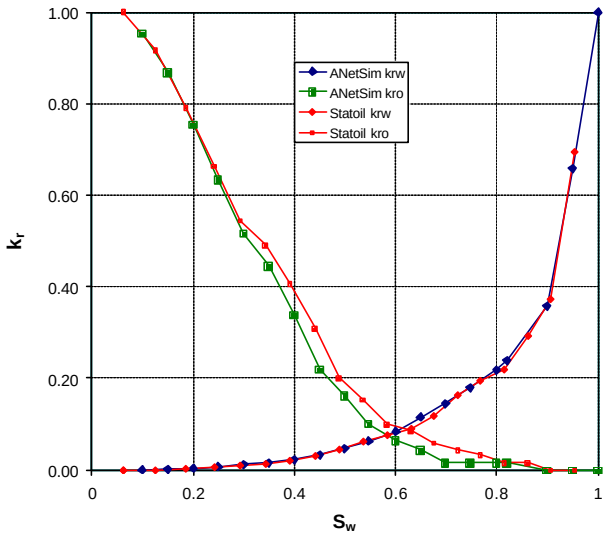

Fig. 18 – Comparison of the calculated drainage relative permeabilities of the Bentheimer sandstone network. Note the slight differences of k_{ro} at the intermediate water saturations. It seems that there might be a subtle difference in the invasion percolation algorithms.

4. Imbibition. The microscopic picture of imbibition in porous media is much more complicated than that of drainage, see, e.g., [10] or [11]. Imbibition with trapping is a special case of bond-and-site invasion percolation, in which the nonwetting fluid clusters must be connected to the outlet. Imbibition is very slow and the invading wetting fluid spans the entire medium through corner films. In contrast, the clusters of nonwetting fluid become trapped when their escape paths are cut-off by the bond-breaking mechanisms.

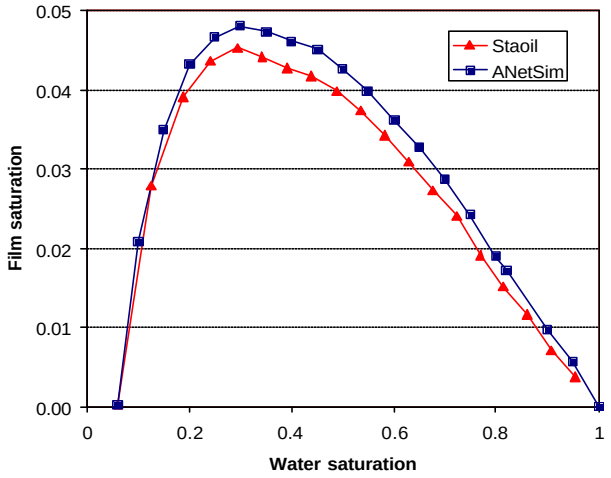

Fig. 19 – The overall saturation of corner filaments versus average water saturation in drainage of the Bentheimer sandstone network. Note that at intermediate water saturations ANetSim predicts consistently higher film saturations.

As capillary pressure decreases, the pore throats fill in order of increasing radius, with the narrowest filling first. The throat filling starts by snap-off (if initially there are no Main Terminal Arc Menisci (MTAM) [15-18]), and then by piston-type imbibition. These two mechanisms can be described by bond invasion percolation and ordinary bond percolation on a dual network [9]. At the same time, the pore bodies attached to the invaded throats are subject to cooperative pore-body filling by the I_n –events. The latter mechanism and snap-off generate compact clusters of wetting fluid. The distribution of events during imbibition of the network in Fig. 5 is shown in **Fig. 20**.

4.1 Piston-type imbibition. If there is contact angle hysteresis, $q_a > q_r$, each corner AM "hinges" about its contact line, pinned at a distance b_i from the corner apex, until the "hinging" contact angle, $q_{h,i}$, exceeds the advancing contact angle, q_a. Thereafter the AM slides at the advancing contact angle, while decreasing its radius of curvature, r_p, to accommodate the current capillary pressure in imbibition. The AM in the sharpest corner slides first while that in the widest corner slides last. The pinned AMs decrease their curvature simply by swelling. The final capillary pressure in primary drainage determines the highest radius of menisci curvature, $r_{pd} = g / P_c^{\max}$.

The maximum advancing contact angle at which spontaneous piston-type imbibition can occur,

$$\cos q_{a,\max} \approx \frac{-4G\sum_{i=1}^{3}\cos(q_r + b_i)}{P_{c,\max} r/g - \cos q_r + 12G\sin q_r}, \qquad (18)$$

depends on the pore geometry, receding contact angle and the maximum capillary pressure in primary drainage.

In a triangular pore, the threshold capillary pressure in spontaneous imbibition, i.e., for $q_a \le q_{a,\max}$, with contact angle hysteresis can be calculated by solving the following system of seven nonlinear algebraic equations in $q_{h,i}$, a_i, $i = 1,2,3$ and r_p:

$$q_{h,i} = \begin{cases} \arccos\left[\frac{r_{pd}}{r_p}\cos(q_r + b_i)\right] - b_i, \text{ if } q_{h,i} \le q_a \\ q_a, \text{ if } q_{h,i} > q_a \end{cases} \quad i = 1, 2, 3$$

$$b_i = \begin{cases} r_{pd}\frac{\cos(q_r + b_i)}{\sin b_i}, \text{ if } q_{h,i} \le q_a \\ r_p \frac{\cos(q_a + b_i)}{\sin b_i}, \text{ if } q_{h,i} > q_a \end{cases} \quad i = 1, 2, 3$$

$$a_i = \begin{cases} \arcsin\left(\frac{b_i}{r_p}\sin b_i\right), \text{ if } q_{h,i} \le q_a \\ p/2 - q_a - b_i, \text{ if } q_{h,i} > q_a \end{cases} \quad i = 1, 2, 3 \qquad (19)$$

$$r_p = \frac{\frac{r^2}{4G} - r_p\sum_{i=1}^{3} b_i \cos q_{h,i} + r_p^2\sum_{i=1}^{3}(\frac{p}{2} - q_{h,i} - b_i)}{2r_p\sum_{i=1}^{3} a_i + \left(\frac{r}{2G} - 2\sum_{i=1}^{3} b_i\right)\cos q_a}$$

The threshold capillary pressure in piston-type imbibition is then $P^e_{cPT} = g/r_p$.

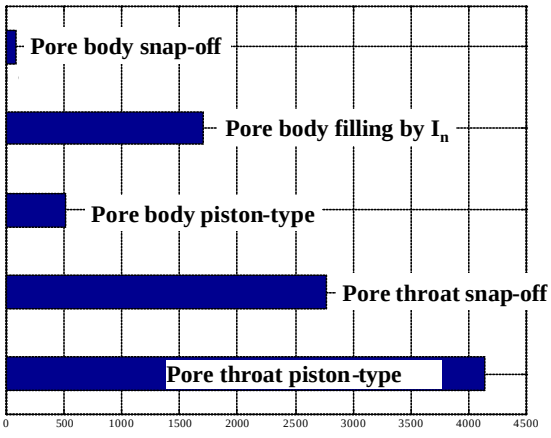

Fig. 20 – The numbers of pore-level events during imbibition of the Bentheimer sandstone network.

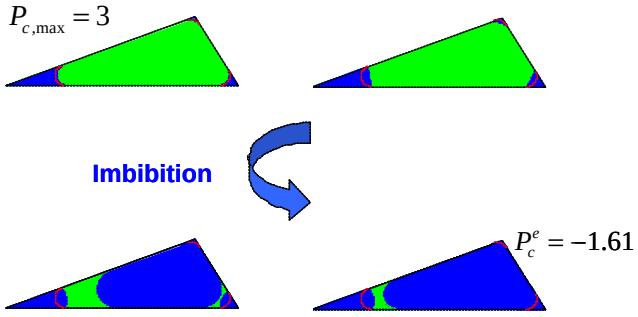

Fig. 21 – Piston-type imbibition with extreme contact angle hysteresis. When the main terminal arc meniscus invades, oil films are created and ultimately squeezed out of the pore.

If contact angle hysteresis is too large, the corner menisci remain pinned, while the MTAM is forced into the pore at a negative capillary pressure, as in primary drainage. When $q_a \ge p/2 + \max(b_i)$, imbibition is forced and intermediate oil films may be created if the maximum capillary pressure in drainage is high enough, **Fig. 21**. In this case, the threshold capillary pressure in piston-type imbibition is obtained from Eq. (15) with q_r replaced with q_a.

When $q_{a,\max} < q_a < p/2 + \max(b_i)$, geometry prevents the creation of intermediate films and the MTAM is forced into the pore when each of its radii of curvature equals $r/\cos q_a$:

$$P^e_{c,PT} = \frac{2g\cos q_a}{r}. \qquad (20)$$

Note that in piston-type drainage and imbibition, each pore behaves as a highly nonlinear valve with threshold and hysteresis that is proportional to the contact angle hysteresis, **Fig. 22**.

4.2. Cooperative pore body filling. The largest radius of curvature of a water-oil interface in a pore body and its oil-filled pore throats defines the threshold capillary pressure necessary to fill that pore body. Thus, this threshold pressure never exceeds that of piston-type invasion of a connecting pore throat filled with oil. The required radius of curvature depends on the size of the pore body and on the number and spatial distribution of connecting pore throats filled with oil. For a pore body with a coordination number *z*, there is *z-1* such pore-body filling mechanisms, Fig. 4. We refer to them as I_1 through I_{z-1}. If only one of the connecting throats contains oil (i.e., the mechanism is I_1), the pore body filling

is similar to that of a piston-type invasion described above and the threshold pressure is almost the same.

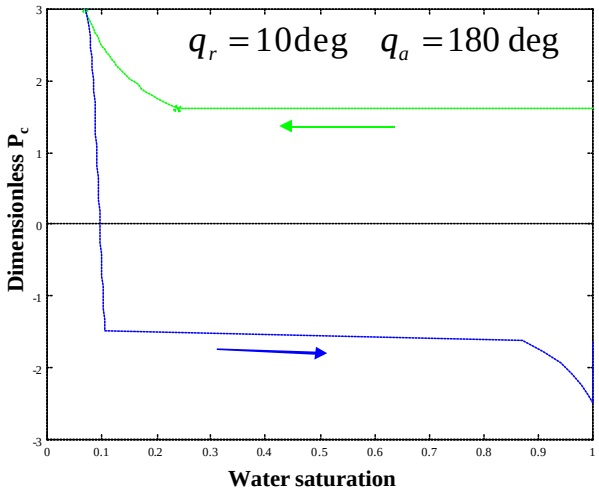

Fig. 22 – The capillary pressures in drainage and piston-type imbibition of the triangular pore shown in Fig. 21. Note the nonlinear pore behavior and large capillary pressure hysteresis resulting from the contact angle hysteresis. The right-most part of the imbibition curve follows the collapse of intermediate oil films.

The threshold pressure for the I_2 to I_{z-1} mechanisms are more complex. Blunt [20] has presented a parametric model for these mechanisms. If $q_a < q_{a,\max}$, the mean radius of curvature for filling by an I_n mechanism is calculated as

$$R_n = \frac{1}{\cos q_a}\left(r_0 + \sum_{i=1}^{n} a_i r_i x_i \right), \qquad (21)$$

where r_0 is the pore body radius, r_i are the radii of the oil-filled pore throats, a_i are geometrical constants, and x_i are random numbers between zero and one. The threshold pore filling capillary pressure for the I_n mechanism is then

$$P^e_{c,n} = \frac{2g}{R_n}. \qquad (22)$$

Improving on this idea, we propose the following model of cooperative pore-body filling. For an I_2 event, the effective radius of curvature is equal to

$$R_2 = r_o + w_1^{(2)} r_1 + w_2^{(2)} r_2, \qquad (23)$$

where r_o is the pore body radius, r_1 and r_2 are the radii of the oil-filled pore throats that participate in the event, and $w_1^{(2)}$ and $w_2^{(2)}$ are the throat radii weights for the I_2 event. These weights in principle could be calculated from the geometry of the pore body and the pore throats involved in a particular I_2 event. Because we do not know this geometry exactly, we may assume that

$$R_2 = r_0 + w_{1,2}^{(2)}(r_1 + r_2). \qquad (24)$$

Equation (24) still requires us to recalculate the effective radius of curvature for every I_2 event, depending on which particular two pore throats are involved. To simplify this procedure further, we may pick all the combinations of throat radii pairs, each with a random weight, normalize them, and endow the average with a single weight:

$$R_2 = r_0 + w^{(2)} \frac{\sum_{jk\,pairs} rand_{jk}(r_j + r_k)}{\sum_{j,k} rand_{jk}}, \qquad (25)$$

where for each combination of throats *j* and *k*, $rand_{jk}$ is the uniform random weight between zero and one, and the normalizing factor in the denominator is the sum of the random weights. Now the common weight, $w^{(2)}$, signifies the relative importance given to the I_2 mechanism relative to the I_3 mechanism and so on. The consecutive weights are found by numerical experimentation. The proposed model yields results similar to those of Blunt's model [20] with Øren *et al.'s* weights [10] when its weights are

$$w^{(2)} = 0.72,\ w^{(3)} = 0.45,\ w^{(4)} = 1.2,\ w^{(5)} = 1.5,\ w^{(n>5)} = 5. \qquad (26)$$

Fig. 23 compares the distribution of threshold capillary pressures for type I_4 events with those for piston-type invasion of the Bentheimer sandstone network. Note that the respective capillary pressures are lower that those for piston-type imbibition and the I_4 events are therefore less likely to occur.

4.3 Snap-off. Snap-off is the invasion of an oil-filled pore by water AMs, which always exist in the corners of pore bodies and throats. If there is no contact angle hysteresis, the AMs advance smoothly along the pore walls as the capillary pressure decreases. At a critical point, three of these AMs fuse together, become unstable and the entire cross-section of the pore fills with water, cutting the oil filament into two parts. The threshold capillary entry-pressure in piston-type imbibition is always higher that that for snap-off; therefore, snap-off occurs *only* when piston-type displacement is *impossible* for topological reasons, i.e., when there is no

water/oil MTAM waiting at the pore end.

For a strongly water wet system, the snap-off instability occurs at a threshold capillary pressure of

$$P_{cSO}^{e} = \frac{g_{ow}}{r}. \qquad (27)$$

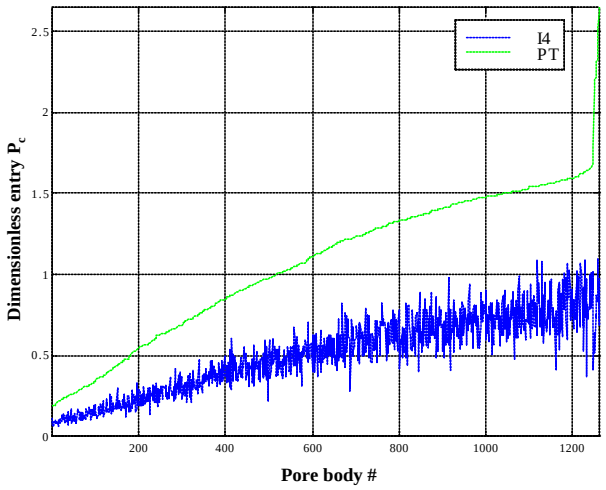

Fig. 23 – The threshold capillary pressures for type I_4 cooperative pore-body filling sorted in order of the increasing corresponding piston-type threshold pressures. Note the stochastic noise introduced by the parametric model.

With contact angle hysteresis, the AMs remain pinned at the positions established at the maximum capillary pressure in drainage, $P_{c,\max}$, until the hinging angle in the sharpest corner equals q_a. Subsequent decrease of capillary pressure causes the sharpest corner's AM to advance towards the center of the pore. Eventually the advancing AM meets another one in the second sharpest corner (at the triangular pore base), causing snap-off. If $q_a < p/2 - \min(b_i)$, the AM in the sharpest corner advances and merges with the other menisci at a positive capillary pressure. In this case, snap-off is spontaneous.

We calculate the threshold capillary entry-pressure for snap-off with contact angle hysteresis, and $q_a < p/2 - \min(b_i) = p/2 - b_{\min}$, by starting from the threshold capillary pressure in piston-type imbibition. Given the initial values of $r_{so} = r_p$ and $q_{h,i}$, obtained from Eqs. (19), we lower the capillary pressure gradually by increasing the meniscus radius and calculate the corresponding hinging angles, $q_{h,i}$, and the meniscus-to-vertex distances, b_i, from Eqs. (19). We then perform the following checks:

$$\begin{aligned} b_1(r_{so_1}, q_{h,1}) + b_2(r_{so_1}, q_{h,2}) &< l_1 = r\left(\cot b_1 + \cot b_2\right), \\ b_2(r_{so_2}, q_{h,2}) + b_3(r_{so_2}, q_{h,3}) &< l_2 = r\left(\cot b_2 + \cot b_3\right), \\ b_1(r_{so_3}, q_{h,1}) + b_3(r_{so_3}, q_{h,3}) &< l_3 = r\left(\cot b_1 + \cot b_3\right), \end{aligned} \qquad (28)$$

where l_i are the lengths of triangle sides expressed through the inscribed circle radius and the corner half-angles. If one or more of conditions in Eq. (28) is violated, two or three of the AMs have met and snap-off has occurred. Solving for the equality signs in each of the conditions in Eq. (28), yields three different radii of the menisci, $r_{SO_i}, i = 1,2,3$. The threshold capillary entry-pressure for snap-off occurs at the minimum radius, i.e., at the highest possible capillary pressure. Note that our procedure is somewhat different and more symmetric than that proposed in [10]. Also, note that for $q_a = p/2 - b_{\min}$ the threshold capillary entry-pressure for snap-off is zero (a flat meniscus in the sharpest corner advances). Therefore, in contrast to piston-type imbibition, spontaneous imbibition by snap-off occurs <u>only</u> for $q_a < p/2$.

If $q_a > p/2 - \min(b_i) = p/2 - b_{\min}$, all three AMs are convex, their curvatures are negative and water invasion is forced. Once the hinging angle in the sharpest corner has increased to q_a, its AM advances towards the center of the pore and the absolute value of its curvature decreases. This situation is analogous to the cause of instability of three concave menisci that met. The convex AM is thus unstable and the part of the pore in which the instability has occurred immediately fills with water. The threshold pressure for this snap-off event depends on the curvature of the AM when it begins to move:

$$r_{so}\cos(q_a + b_{\min}) = r_{pd}\cos(q_r + b_{\min}), \qquad (29)$$

and the threshold capillary entry-pressure is given by

$$P_c^e = \frac{g_{ow}}{r_{so}} = P_{c,\max}\frac{\cos(q_a + b_{\min})}{\cos(q_r + b_{\min})}, \quad q_a < p - b_{\min}. \qquad (30)$$

Otherwise, the numerator in Eq. (30) is replaced by its smallest possible value ($\cos p = -1$) and

$$P_c^e = \frac{g_{ow}}{r_{so}} = P_{c,\max}\frac{-1}{\cos(q_r + b_{\min})}, \quad q_a \geq p - b_{\min}. \qquad (31)$$

Equation (31) holds because the capillary entry pressure versus water saturation curve has a global minimum when

$q_a + b_{\min} = p$. This minimum corresponds to the AM forming a half-circle. At higher water saturations, meniscus curvature decreases and the meniscus becomes unstable [21]. For larger advancing contact angles, this unstable branch cannot be reached; hence, Eq. (31) comes into play.

Fig. 24 depicts snap-off with contact angle hysteresis. The AM in the sharpest corner slides first, followed by the meniscus in the intermediate corner. The miniscule meniscus in the widest corner remains pinned; thus, the first two menisci touch resulting in snap-off.

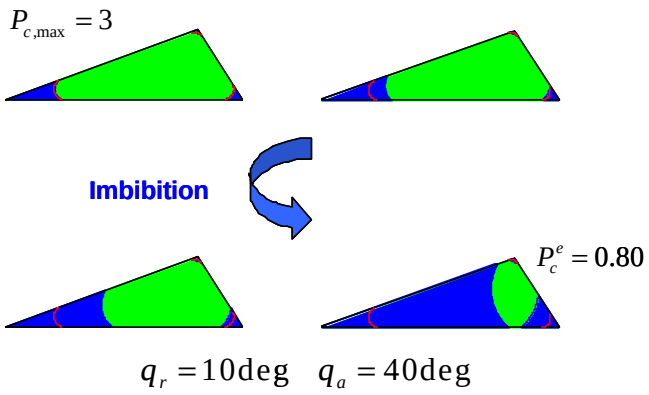

Fig. 24 – Snap-off with contact angle hysteresis. The AM in the widest corner remains pinned.

The corresponding capillary pressures in the same pore are shown in **Fig. 25**. Because there is no MTAM waiting to invade, capillary pressure in imbibition falls to a low value, at which the two menisci in Fig. 24 touch, snap-off occurs and capillary pressure returns to its threshold value in drainage. As in piston-type imbibition, the pore behaves as a nonlinear valve with threshold and hysteresis.

4.4 Imbibition Results. The calculated capillary pressure curve in imbibition of the Bentheimer sandstone network is shown in **Fig. 26** and the corresponding relative permeabilities in **Fig. 27**. The calculated residual oil saturation to water is 31%. Agreement with the Statoil calculations of capillary pressure and experimental relative permeabilities is excellent.

5. Implementation. ANetSim has been implemented in MATLAB® [14] and runs on any platform with MATLAB installed on it. In particular, all the results presented in this paper have been obtained on a 266 MHz Dell Inspiron 3000 Notebook with 144MB of memory. Most of the subroutines in ANetSim have been vectorized and take full advantage of vector- and matrix-handling capabilities of MATLAB. The CPU time for drainage and imbibition calculations on the Bentheimer sandstone network are shown in **Fig. 28** and **Fig. 29**. The drainage calculations are quite competitive; it takes about 20 minutes to generate the full suite of calculations for the Bentheimer sandstone network.

The imbibition calculations are much slower, about 5 hours of CPU time, mostly because of time spent in a labeling subroutine that finds all clusters of the nonwetting phase connected to the outlet. This subroutine contains nested if statements, which disrupt MATLAB vectorization. In the future, the cluster subroutine will be rewritten in C and linked to the MATLAB code.

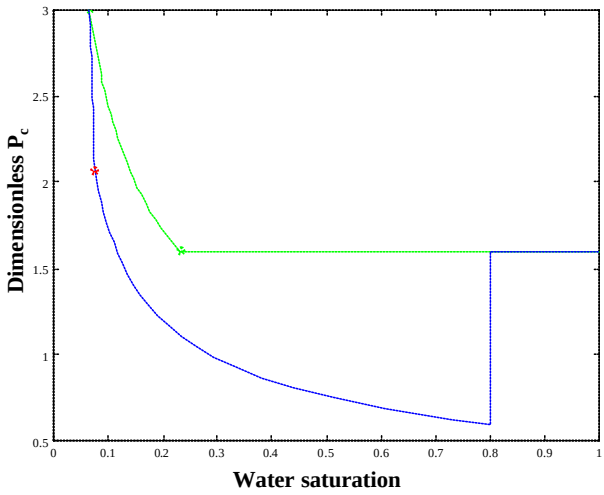

Fig. 25 – Capillary pressure curves in drainage and imbibition with snap-off shown in Fig. 24.

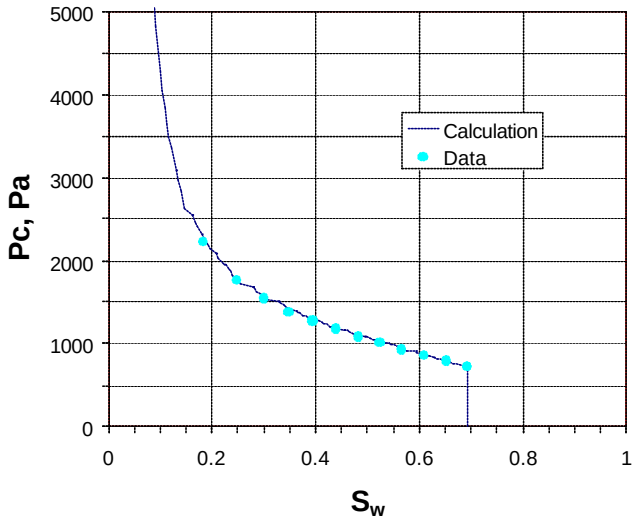

Fig. 26 – The capillary pressure curve in imbibition of the Bentheimer sandstone network. The points denote the Statoil calculations.

6. Current and future work. First, we are working on extracting the relevant pore network description from micro-CT and NMR images. **Fig. 30** through **Fig. 32** illustrate our present capability of extracting the relevant pore network data from an NMR image of a small sample of Bentheimer sandstone. For image analysis, we use the public domain code

developed by Lindquist [22]. Thus far, we have developed an interface between his code and MATLAB, which visualizes network analysis. In the future, we plan to develop a fully automatic tool to extract pore network information for ANetSim.

Second, we are developing the numerical models of sandstone deposition, compaction and cementation. Thus far, we have developed a very efficient algorithm of depositing spherical sand grains in a low-energy (local minimum of potential energy) or high-energy (global minimum) environment and pre-compacting them. Deposition and compaction of 1024 grains takes a few minutes on a laptop, **Fig. 33**. The "images" of these sandstones will then be analyzed and fed into ANetSim.

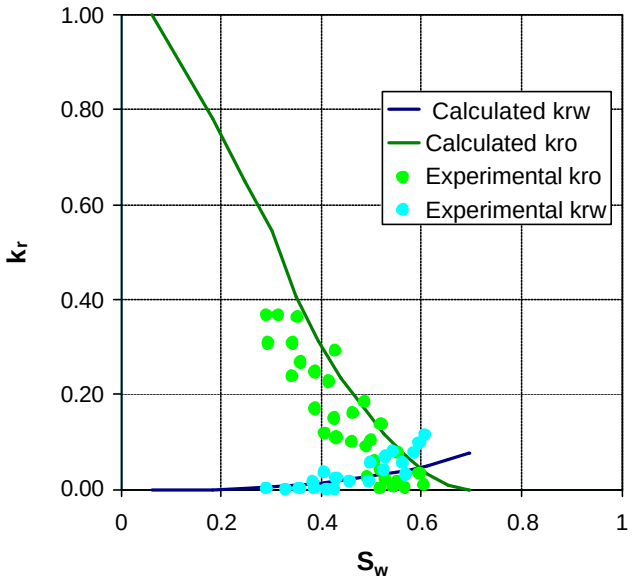

Fig. 27 – The relative permeability curves in imbibition of the Bentheimer sandstone network. The experimental points are from [10], their Fig. 14.

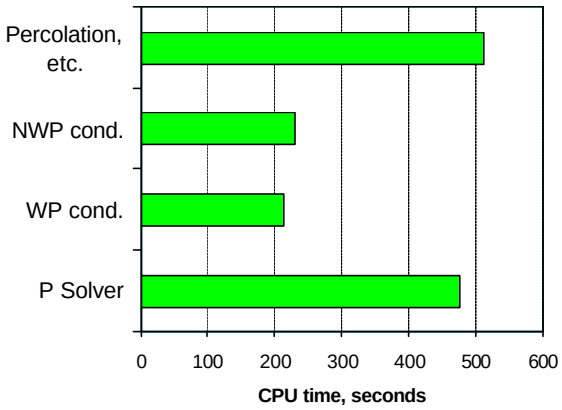

Fig. 28 – CPU time for the Bentheimer sandstone drainage calculations on a 266MHz Dell Inspiron 3000 Notebook with MATLAB 5.2.1 and Windows NT 4.0/ SP 5. Note that the pressure solver is very competitive with the compiled C or FORTRAN programs. *NWP cond*. stands for the calculation of the nonwetting phase hydraulic conductances, etc.

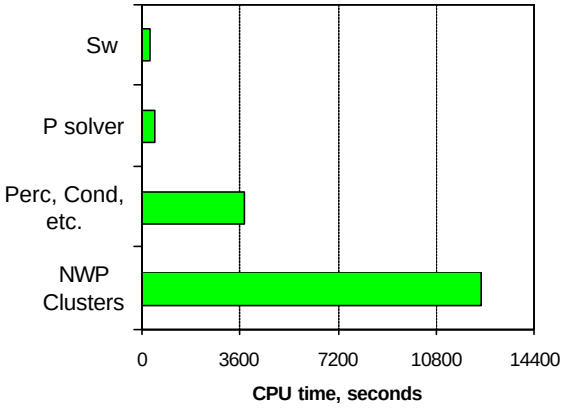

Fig. 29 – CPU time for the Bentheimer sandstone imbibition calculations on a 266MHz Dell Inspiron 3000 Notebook with MATLAB 5.2.1 and Windows NT 4.0/SP 5. Note that majority of CPU time is spent on determining the nonwetting phase cluster connectivity to the outlet. *Perc, Cond, etc*., stands for the imbibition percolation algorithm, the calculation of hydraulic conductances, and the setup of the pressure equations for each phase.

Third, we are collaborating with Dr. Such at the Institute of Oil and Gas Mining, Krakow, Poland, to determine by experiment the fractal dimensions of porosity in various sandstones, and use these dimensions in ANetSim to model drainage at high capillary pressures. The fractal structure of pore space can be characterized using mercury porosimetry as suggested by Turcotte [23]. A generalized Menger's sponge [24] can be used in the modeling. Preliminary results are shown in **Fig. 34**.

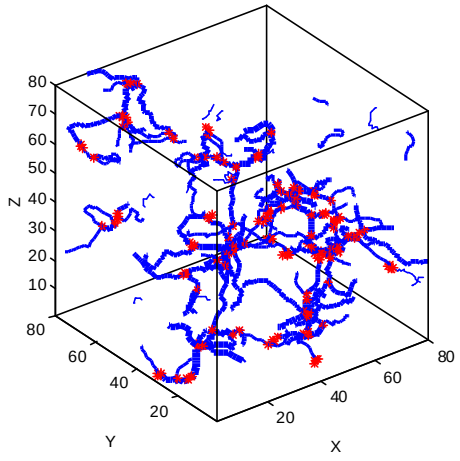

Fig. 30 – Extraction of pore bodies and the connecting pore throats from a small NMR image of Bentheimer sandstone acquired by L. Tomutsa at the Lawrence Berkeley National Laboratory (LBNL). The extraction was

performed by A. De, LBNL.

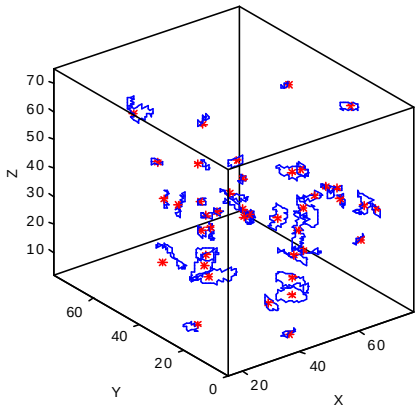

Fig. 31 – A. De's extraction of average pore throat shapes from a small NMR image of Bentheimer sandstone acquired by L. Tomutsa at LBNL.

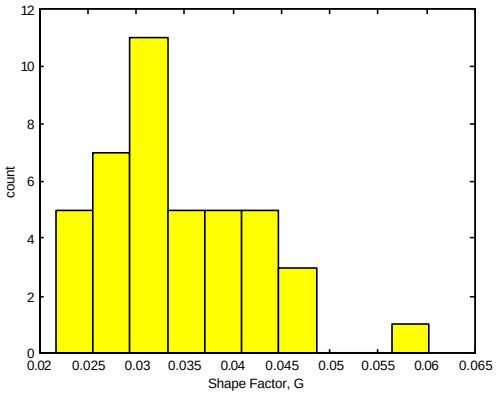

Fig. 32 – Distribution of the pore-throat shape factors in Fig. 31.

8. Conclusions. A quasi-static pore network simulator, "ANetSim," of two-phase drainage and imbibition has been written and verified against the state-of-the-art, proprietary simulator of Statoil. A complete description of all pore-level events has been incorporated. ANetSim can predict successfully the absolute rock permeability and the relative permeabilities in primary and higher-order drainage processes. Secondary and higher-order imbibition relative permeabilities can also be predicted. Pore-by-pore drainage and imbibition capillary pressure curves, including their unstable branches can be obtained. The simulator predictions are in good agreement with Statoil's calculations and experiment. Thus, pore network simulators can be used in quantitative predictions of rock properties. Image analysis must be used to convert the imaged pore space geometry into an equivalent pore network.

The rule-based pore network simulators with complete physics of quasi-static drainage and imbibition are still rare. ANetSim, in particular, has the following features:

- Arbitrary triangular, rectangular and elliptic cross-sections of pore bodies (nodes) and throats (links)
- Arbitrary spatial distribution of connectivity between nodes and links
- Arbitrary distribution of rock wettability captured by the variable receding and advancing contact angles
- Corner film flow with arbitrary contact angle hysteresis
- Piston-type displacement and snap-off with arbitrary contact angles and for arbitrary conditions after primary drainage
- Cooperative pore body filling (I_n mechanisms)
- Models of spatial distribution of altered wettability
- Efficient oil-cluster checking algorithm
- Efficient pore-by-pore invasion percolation algorithm with all site and bond-breaking mechanisms
- Intermediate oil films sandwiched between pinned corner menisci and central filaments of invading water (almost done)
- Fractal model of clay microporosity (in progress)

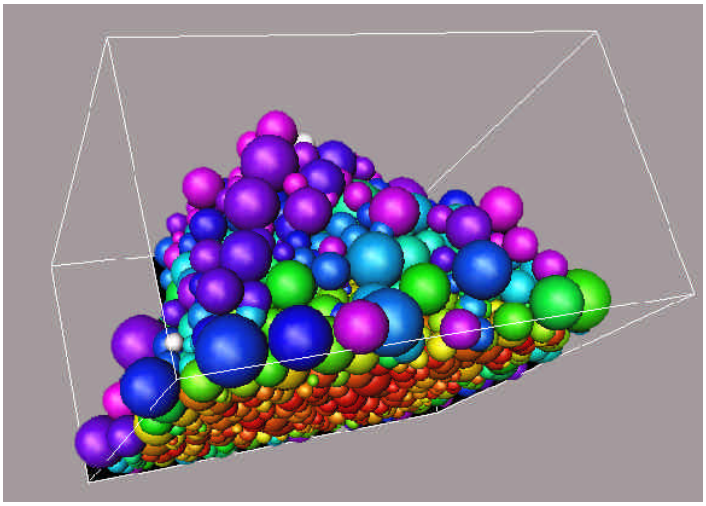

Fig. 33 – Deposition and compaction of 1024 spherical sand grains in low energy environment, OpenInventor rendering of MATLAB output by T.W. Patzek. The MATLAB deposition algorithm is by A. De and K. Hildenbrand, LBNL.

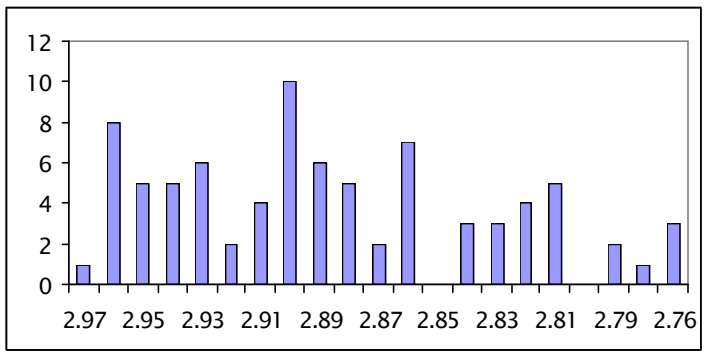

Fig. 34 – Number of samples vs. fractal dimension of pore space in sandstones [25].

In return, ANetSim can calculate:

- Full capillary pressure curves under primary drainage and secondary imbibition
- Higher-order capillary pressure scanning loops
- Relative permeabilities under the respective drainage and imbibition loops
- Residual nonwetting phase saturation
- Formation resistivity factor

9. Acknowledgments. I would like to thank Dr. Paal-Eric Øren of Statoil for hosting me in Trondheim, Norway, during the Fall 1998 sabbatical leave from U.C. Berkeley, and for helping in the development and debugging of my pore network simulator. This work was sponsored in parts by Statoil, U.C. Berkeley and PV Technologies, Inc. Dr. A. De and K. Hildenbrand are working on the network extraction and sedimentation models. The pore images have been provided by L. Myer and L. Tomutsa, who are supported by the Department of Energy, Assistant Secretary for Fossil Energy, Office of Natural Gas and Petroleum Technologies, National Petroleum Technology Office, Contract No. DEA-AC03-26SF00098.

10. References.

1. Morrison, P., Morrison, Ph., and the Office of Eames, Ch., and R., *Powers of Ten*. Scientific American Library. 1982, New York: HPHLP. 150.
2. Doolen, G.D., Senior Editor, ed. *Lattice gas methods for partial differential equations*. The Advanced Book Program. 1990, Addison-Wesley Publ. Co.: Redwood City, CA.
3. Xu, B., Kamath, J., Yortsos, Y. C., and Lee, S. H., *Use of pore-network models to simulate laboratory corefloods in a heterogeneous carbonate sample*. SPEJ, 1999. **4**(3): p. 179-186.
4. Gaylord, R.J., and Wellin, P. R., *Computer Simulations with Mathematica - Explorations in Complex Physical and Biological Systems*. TELOS - The electronic Library of Science. 1995, Santa Clara: Springer-Verlag.
5. de Gennes, P.G., *Percolation - a new unifying concept*. La Recherche, 1980. **7**: p. 919-26.
6. Wilkinson, D., and Williamsen, J. F., *Invasion Percolation: A new form of percolation theory*. J. Phys. A. Math Gen., 1983. **16**: p. 3365-3376.
7. Dias, M.M., and Wilkinson, D., *Percolation with trapping*. J., Phys. A: Math Gen., 1986. **19**: p. 3131-3146.
8. Lenormand, R., Zarcone, C., and Sarr, A., *Mechanisms of Displacement of One Fluid by Another in a Network of Capillary Ducts*. J. Fluid. Mech., 1983. **135**: p. 337-353.
9. Lenormand, R., *Pattern growth and fluid displacements through porous media*. Physica A, 1986. **140**: p. 114-123.
10. Øren, P.-E., Bakke, S., and Arntzen, O. J., *Extending Predictive Capabilities to Network Models*. SPEJ, 1998. **3**(4): p. 324-336.
11. Patzek, T.W., *E240- Fundamentals of Multiphase Flow in Porous Media*. First ed. 1999, Berkeley: U.C. Berkeley. 250.
12. Mason, G., and Morrow, N. R., *Capillary Behavior of a Perfectly Wetting Liquid in Irregular Triangular Tubes*. J. Colloid and Interface Science, 1991. **141**: p. 262.
13. Kristensen, J.G., *The Universal Scaling of Conductance in Laminar Film Flow of Wetting Liquid along the Corners of an Angular Pore*, in *MSME*. 1999, UC Berkeley: Berkeley.
14. Mathworks, I., *MATLAB - The Language of Technical Computing*, 1998, MathWorks, Inc.: Natick, MA.
15. Mayer, R.P., and Stowe, R. A., *Mercury-Porosimetry Breakthrough Pressure for Penetration between Packed Spheres*. J. Colloid and Interface Science, 1965. **30**: p. 893-911.
16. Princen, H.M., *Capillary Phenomena in Assemblies of Parallel Cylinders. I. Capillary Rise between Two Cylinders*. J. Colloid and Interface Science, 1969. **30**: p. 60.
17. Princen, H.M., *Capillary Phenomena in Assemblies of Parallel Cylinders. II. Capillary Rise in Systems with More than Two Cylinders*. J. Colloid and Interface Science, 1969. **30**: p. 359.
18. Princen, H.M., *Capillary Phenomena in Assemblies of Parallel Cylinders. III. Liquid Columns between Horizontal Parallel Cylinders*. J. Colloid and Interface Science, 1970. **34**: p. 171.
19. Patzek, T.W., *AMSim - Single Pore Meniscus Equilibria Simulator*, 1998, T. W. Patzek: Berkeley.
20. Blunt, M.J., *Pore Level Modeling of the Effects of Wettability*. SPEJ, 1997. **December**: p. 449.
21. Brown, R.A., *The Shape and Stability of Three Dimensional Interfaces*, in *ChemE*. 1979, University of Minnesota: Minneapolis.
22. Lindquist, W.B., *3DMA - Medial Axis Analysis of 3D, Biphase Images*, 1999, Department of Applied Mathematics and Statistics, SUNY: Stony Brook, N. Y.
23. Turcotte, D.L., *Fractals and Chaos in Geology and Geophysics*. 1997, Cambridge: Cambridge University Press.
24. Mandelbrot, B.B., *The Fractal Geometry of Nature*. 1977, New York: Freeman and Comp.
25. Such, P. *Use of Fractal Analysis in the Characterization of Flow Properties of Reservoir Rocks (in Polish).* in *10th International Conference, New Methods in Petroleum, Drilling,*

and Reservoir Engineering. 1999. Krakow: University of Mining and Metallurgy.